Fabrication of SnO₂/α-Fe₂O₃, SnO₂/α-Fe₂O₃−PB Heterostructure Thin Films: Enhanced Photodegradation and Peroxide Sensing

Sumanta Jana and Anup Mondal*

Department of Chemistry, Indian Institute of Engineering Science and Technology, Shibpur, Howrah 711103, WB India

Ⓢ *Supporting Information*

ABSTRACT: We report the synthesis of SnO₂/α-Fe₂O₃ heterostructure thin films by employing two-step processes: galvanic and chemical deposition. Fe₂O₃ is a narrow band gap semiconductor and has short hole diffusion length. Therefore, the photogenerated electrons and holes are not easy to separate in Fe₂O₃. Combining Fe₂O₃ to SnO₂, a wide-energy-gap semi-conductor having suitable valence band and conduction band position is a promising candidate for the photo catalysts. The chemical modification of this heterostructure was achieved by electro-active Prussian blue (PB) molecule. The photocatalytic activities of SnO₂, α-Fe₂O₃, SnO₂/α-Fe₂O₃, and SnO₂/α-Fe₂O₃−PB thin films were investigated for organic dye degradation. It was observed that the coupled and combined modified systems showed better reactivity compared to individual single-component materials. The electrocatalytic activity of the synthesized thin films has also been studied where hydrogen peroxide (H₂O₂) was taken as a model compound. Amperometric study also reveals that the couple and combined modified thin films are more effective at sensing hydrogen peroxide (H₂O₂) than single-component materials.

KEYWORDS: thin films, heterostructures, oxides, photocatalyst, photodegradation, sensor
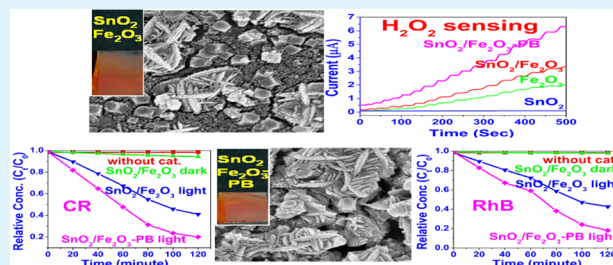
1. INTRODUCTION

Recently, metal oxide semiconductors have given much attention because of its high stability and surface active chemical and electronic properties. Several simple metal oxide semiconductors, e.g., WO₃,[1] ZnO,[2] NiO,[3] TiO₂,[4] SnO₂,[5] etc., have sufficient band gap energy to catalyze photochemical reactions and are used widely for environmental awareness.[6] There are a large number of pollutants that are harmful to the environment, hazardous to human health, safety, and difficult to decompose. For environmental remediation, lots of research on photocatalysis has been started on metal oxide semiconductors because of their high stability, availability, nontoxicity.[7] Among the metal oxide semiconductors, tin oxide (SnO₂) has been studied enormously becaue of its high stability and tunable optical, electrical, and optoelectronic properties.[8] The material is used extensively as electrode material in Li-ion battery,[9] solar cell and dye-sensitized solar cells,[10] solid-state gas sensors,[11] photoelectrochemical material,[12] photo catalysis,[13] etc. Because of its unique photoelectronic properties, nontoxicity, and chemical stability, it is widely used as photocatalyst.[14,15] On the other hand; Fe₂O₃ is a narrow band gap n-type semiconductor (~2.2 eV), used extensively as electrochemical electrodes, gas sensors and photocatalysts.[16,17]As a narrow band gap semiconductor, Fe₂O₃ shows a wide photoelectrochemical response, but the holes in valence band (V_B) have low oxidation ability because of short hole diffusion length.[18] On the other hand, SnO₂ has a low valence band edge potential and therefore has no absorption to the light under visible region becaue of its wide band gap (~3.8 eV).[19] Now, the

photocatalytic activity can greatly be enhanced by combining Fe₂O₃ to another semiconductor having suitable valence band and conduction band. SnO₂, a direct band gap n-type semiconductor having outstanding electrical and optical properties, is a possible candidate for this combination.[20,21] Various Fe₂O₃/SnO₂ heterostructures were successfully synthe-sized by different techniques and used in selective purposes. Zhang et al. had nicely prepared an assemble of SnO₂ nanorod arrays hierarchically on the surface of α-Fe₂O₃ nanotubes.[22] Fe₂O₃−SnO₂ synthesized by mechanical alloying shows better reactivity in sensing ethanol gas selectively compared to carbon monoxide and hydrogen.[23] The same heterostructure thin film synthesized by wet chemical method is able to sense hydrogen sulfide and liquefied petroleum gas selectively.[24,25] Core−shell α-Fe₂O₃/SnO₂ nanorods synthesized by Chen et al. used selectively in ethanol sensing.[26] Branched SnO₂−α-Fe₂O₃, synthesized by hydrothermal method, showed effective photo-degradation of MB dye[27] and the same heterostructure synthesized by similar hydrothermal route was used to sense methane, carbon monoxide.[28] Heterostructure generated by coprecipitation method shows high electron−hole separation.[28] A necklacelike SnO₂/α-Fe₂O₃ hierarchical heterostructure fabricated by chemical vapor deposition method, showed effective phodegradtion of MB dye.[29] Burda et al. and Astruc et al.[30,31] have nicely explained the catalytic activities of Fe₂O₃
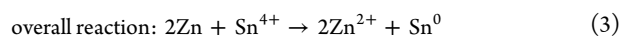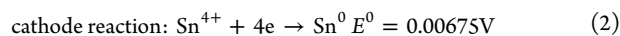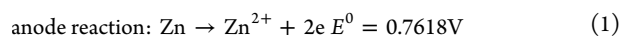
nanoparticles. But the peroxidase activity of Fe_2O_3 is still underdeveloped because of a lack of sufficient ferrous ions. Hence, to investigate the peroxidase activity of Fe_2O_3, it is immediately needed a modification with Prussian Blue (PB).[32] PB provides necessary ferrous ions which facilates the catalytic reaction and accelerates electron transfer.[33] This unique feature will be helpful to catalyze the reduction of hydrogen peroxide.[34]

In this article, we have used a galvanic technique to synthesize nanostructure SnO_2 thin films on transparent conducting oxide (TCO) coated glass substrates. To synthesize α-Fe_2O_3 on SnO_2, chemical deposition technique has been used. Chemical modification of the heterostructure, i.e., SnO_2/α-Fe_2O_3 was accomplished by prussian blue (PB). Photocatalytic and electrocatalytic activities of these heterostructures have been studied. Photocatalytic activities of SnO_2, α-Fe_2O_3, SnO_2/α-Fe_2O_3, and SnO_2/α-Fe_2O_3–PB thin films were monitored for Congo-red (toxic chemical and common pollutant of industrial water) and Rhodamine B dye. An enhanced photodegradation was achieved for the coupled (SnO_2/α-Fe_2O_3) and modified system (SnO_2/α-Fe_2O_3–PB), compared to the single-component system. Electrocatalytic activity of the synthesized materials again confirmed that the coupled and modified thin films show better response toward hydrogen peroxide (H_2O_2) sensing compare to each single component.

2. EXPERIMENTAL SECTION

Materials and instruments are given in the Supporting Information.

2.1. Synthesis of SnO_2 Thin Films. SnO_2 thin films were synthesized by modifying our previously reported procedures.[35] A properly cleaned TCO glass substrate (glass thickness, 3.2 mm; conducting layer, FTO (fluorine doped tin oxide, SnO_2:F); protective layer, silicon dioxide (SiO_2); resistivity, 10−12 ohm/square) and a Zn strip (99% pure) were vertically clamped into a chemical bath containing 80 mL 0.1 M $SnCl_4$ and 10 mL 0.01 M KNO_3 (as supporting electrolyte). The total volume of the solution was maintained to 100 mL with deionized water and the pH was adjusted to 2.3−2.5 with dilute nitric acid. The Zn strip acted as an easily oxidizable anode and the TCO served as the cathode. The electrodes were short-circuited externally through a copper wire. The deposition was carried out at 80 °C under stirred condition. In the electrochemical cell, Zn^{2+} ions were released from the Zn electrode (anode) to the solution and the electrons that were generated because of this oxidation received short-circuited path and move to the cathode (TCO), where Sn^{4+} gets reduced to elemental tin (Sn^0). Then, H_2O_2 (30%) was added dropwise onto the slightly black surface of TCO and the black surface immediately turned white because of the oxidation of Sn to SnO_2.

$$\text{anode reaction: } Zn \rightarrow Zn^{2+} + 2e \quad E^0 = 0.7618V \tag{1}$$

$$\text{cathode reaction: } Sn^{4+} + 4e \rightarrow Sn^0 \quad E^0 = 0.00675V \tag{2}$$

$$\text{overall reaction: } 2Zn + Sn^{4+} \rightarrow 2Zn^{2+} + Sn^0 \tag{3}$$

H_2O_2 and NO_3^- ions readily dissociate and form nascent oxygen

$$H_2O_2 \rightarrow H_2O + [O] \tag{4}$$

$$NO_3^- \rightarrow NO_2^- + [O] \quad E^0 = 0.01V \tag{5}$$
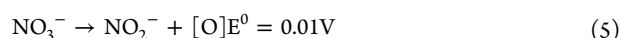
The nascent oxygen [O] generated in reaction (4) and (5) readily reacts with elemental tin (Sn^0) and converts to SnO_2

$$Sn^0 + 2[O] \rightarrow SnO_2 \tag{6}$$

A white transparent layer of SnO_2 was found to be deposited on TCO substrate within 30 min. Here, further annealing of the deposited thin films was not needed. High oxidizing media (presence of H_2O_2 and KNO_3) results complete oxidation of Sn to SnO_2.

2.2. Synthesis of SnO_2/α-Fe_2O_3 Thin Films. α-Fe_2O_3 thin films were deposited onto SnO_2 surfaces following our previously reported chemical deposition procedure.[36] Briefly, equimolar aqueous solutions of (0.01 M) sodium nitropruside and Mohr salt were mixed in a beaker and stirred for 30 min. The final volume was adjusted to 100 mL and pH was maintained in between 2.6 and 2.8 by dilute H_2SO_4. Then, the solution was again stirred for additional 30 min. Now, as-prepared SnO_2 thin films were vertically immersed into the working solution for 24 h. Slow diffusion of the cationic and anionic parts result a bluish green thin layer of hydrated iron nitropruside [Fe[Fe(CN)$_5$(NO)]-1.5H$_2$O] (compound 1) on both sides of the substrate. The deposited films were washed thoroughly with water and layers deposited on back side of SnO_2 surfaces were removed. The deposited iron nitropruside thin films (on SnO_2 layer) were air annealed at 650 °C for 30 min to get the desired α-Fe_2O_3 thin films (TCO/SnO_2/α-Fe_2O_3). The same procedure was repeated for plain TCO substrate to deposit TCO/α-Fe_2O_3 thin films.

2.3. Synthesis of SnO_2/Fe_2O_3–PB Thin Films. The as-prepared SnO_2/α-Fe_2O_3 thin films were dipped into another reaction bath containing 10 mL of 0.10 M K_3[Fe (CN)$_6$] and 10 mL of 0.10 M $FeCl_3$ in 0.01 M HCl solution. After 20 min, the films were taken out from the bath and washed repeatedly with 0.01 M HCl and water. The films were dried at room temperature for several hours. Figure S1 in the Supporting Information shows the photograph of TCO, SnO_2, SnO_2/α-Fe_2O_3, and SnO_2/α-Fe_2O_3–PB thin films. A schematic diagram of the synthetic path is shown in Figure 1 where A, B, C
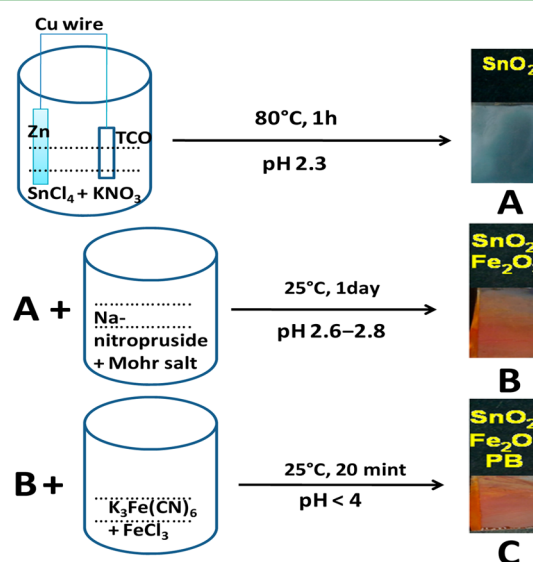

Figure 1. Schematic diagram of different thin film syntheses: A, B, and C represent SnO_2, SnO_2/α-Fe_2O_3, and SnO_2/α-Fe_2O_3–PB thin films.

represent SnO_2, SnO_2/α-Fe_2O_3, and SnO_2/α-Fe_2O_3–PB thin films. Table S1 in the Supporting Information represents EDX percentage of Fe, added during this modification from different solutions.

To prepare Prussian blue "PB", generally ferrous (Fe^{2+}) ions are needed, but in this article we have used Fe^{3+} ions to prepare "PB". This method has earlier been used by several researchers to prepare PB.[32,40] Because in nanoparticles there exist a large ratio of surface to volume, high surface activity, and a high amount of dangling bonds on nanoparticle's surface, the atoms on the surface are apt to absorb ions. Therefore, Fe^{3+} can easily adsorb in the surface and further [Fe(CN)$_6$]$^{3-}$ could also be adsorbed. In the nanoparticle's surface a red-ox couple generates ($Fe^{3+} \leftrightarrow Fe^{2+}$) and HCl medium control the process. At this moment further addition of Fe^{3+} ($FeCl_3$) results a blue color, i.e., "PB".

In diluted HCl medium, the surface charge is positive and [Fe(CN)$_6$]$^{3-}$ could be attracted on the Fe_2O_3 surface for the static electric attraction. Both of the two factors promote the adsorption of [Fe(CN)$_6$]$^{3-}$ rapidly and moment further addition of Fe^{3+} ($FeCl_3$)
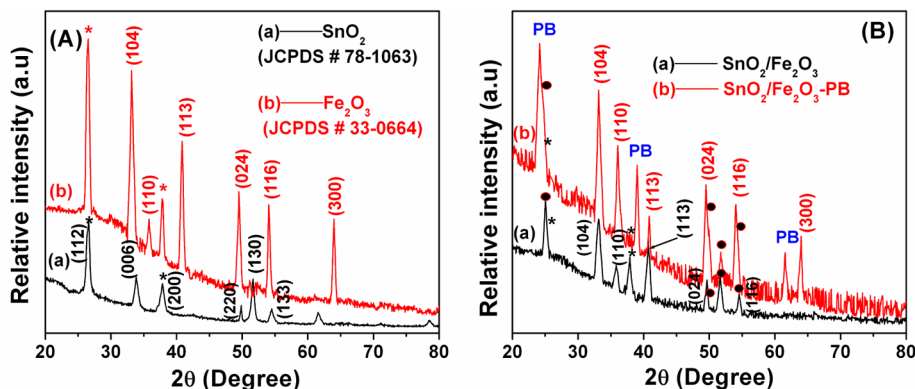
Figure 2. (A) XRD pattern of (a) SnO_2 and (b) α-Fe_2O_3 thin films; * denotes TCO peak. (B) XRD pattern of (a) SnO_2/α-Fe_2O_3 and (b) SnO_2/α-Fe_2O_3−PB thin films. * denotes TCO peak and ● indicates SnO_2 peak.

results a blue color, i.e., "PB" followed by surface red-ox reaction. There may be another way, free Fe^{3+} ($FeCl_3$) ion will combine with $K_3[Fe(CN)_6]$ to form ferriceferricyanide Prussian yellow (PY), which readily converts to PB by reduction.[37]

$$Fe^{3+} + K_3[Fe(CN)_6] \rightarrow \underset{(PY)}{Fe^{3+}[Fe(CN)_6]} \rightarrow \underset{(PB)}{KFe^{3+}[Fe(CN)_6]}$$

$$(7)$$
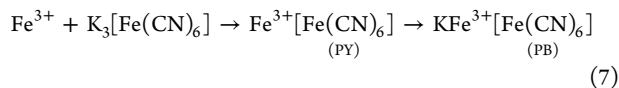
3. RESULTS AND DISCUSSION

Figure 2A(a) shows the X-ray diffraction pattern of SnO_2 thin film on TCO substrate. The major diffractions were observed from (112), (006), (200), (130) planes whose 2θ values matches well with the standard JCPDS values for the orthorhombic structure (JCPDS 78−1063). Figure 2A(b) represents X-ray diffraction pattern of Fe_2O_3 thin film on TCO where diffractions were appeared from (1 0 4), (1 1 0), (1 1 3), (0 2 4), (1 1 6), and (3 0 0) planes. The highest intensity peak appeared from the (1 0 4) plane at $2\theta = 33.15°$. All the 2θ values and intensities match with standard JCPDS 33−0664 of rhombohedra phase. In both cases (a, b) the peaks marked * in the XRD pattern appeared because of the TCO substrate. So, it can be concluded that, on annealing the precursor film (containing compound 1) at 650 °C, thin film of α-Fe_2O_3 was developed. From the XRD pattern; no other phases of iron oxide like β-Fe_2O_3, γ-Fe_2O_3 or Fe_3O_4 were detected. Figure 2B(a) and 2B(b) represent the XRD pattern for SnO_2/α-Fe_2O_3 and SnO_2/α-Fe_2O_3−PB thin films. Here, α-Fe_2O_3 diffractions were observed from (1 0 4), (1 1 0), (1 1 3), (0 2 4), and (1 1 6) planes, which suit the same JCPDS 33−0664.

The modification of SnO_2/α-Fe_2O_3 thin films by prussian blue (PB) was established by XRD. Figure 2B(b) represents the XRD pattern of SnO_2/α-Fe_2O_3−PB films. In the diffraction pattern, along with parent SnO_2 and α-Fe_2O_3 peaks some extra peaks were also observed. The extra peaks were appeared due to insertion of PB into SnO_2/α-Fe_2O_3 heterostructure in accordance to similar observation by Zhang et al.[38] The peaks marked * and ● in this XRD pattern appeared because of the TCO and SnO_2.

Figure 3 represents the FESEM images of (A) SnO_2, (B) α-Fe_2O_3, (C) SnO_2/α-Fe_2O_3, and (D) SnO_2/α-Fe_2O_3−PB modified thin films on TCO substrates. For SnO_2 thin film (Figure 3A), a significant grain growth results in a porous flakelike morphology, uniformly distributed on to the entire TCO substrate. Figure 3B shows the SEM image of Fe_2O_3 nanoparticles on TCO substrate. Uniform spreading of worm
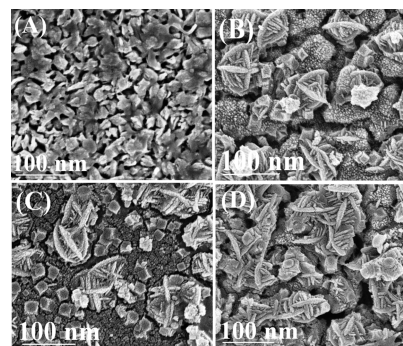

Figure 3. FESEM images of (A) SnO_2, (B) α-Fe_2O_3, (C) SnO_2/α-Fe_2O_3, (D) SnO_2/α-Fe_2O_3−PB thin films.

like dendritic porous nanoparticles is clearly visible from the SEM image.

Figure 3C is the SEM image of SnO_2/α-Fe_2O_3 thin film. Here, similar wormlike Fe_2O_3 nanoparticles are observed with lower SnO_2 layer. Here, the nanoparticles are of much even sizes, and the surfaces are smooth, this benefit will surely influence the inherent properties of materials. From the EDAX analysis the atomic percentage was found to Sn:Fe:O = 14·90:3·16:81·94.

In the case of SnO_2/α-Fe_2O_3−PB modified thin films, uniform porous nanostructure with some agglomeration is detected (Figure 3D). The material is porous and due to extra Fe incorporation lower SnO_2 layer is not visible. The atomic percentage was found to Sn:Fe:O = 14·64:4·65:80·71. So, about 1.49% of extra Fe incorporation was found in the modified system (SnO_2/α-Fe_2O_3−PB) compare to SnO_2/α-Fe_2O_3. Figure S2 (see the Supporting Information) represents the EDX of SnO_2/α-Fe_2O_3 and SnO_2/α-Fe_2O_3−PB thin films. The EDX of modified material (SnO_2/α-Fe_2O_3−PB) shows presence of C and N along with other expected elements. This again confirms the presence of PB in the modified heterostructure. All the synthesized thin films are so stable that we could not collect a minimum amount of powder material for the BET and HRTEM analysis to measure the porosity and exact particle size.

Figure 4A(a) depicts the UV−vis absorption spectrum of SnO_2 thin film. The band gap energy (E_g) was calculated using the conventional Tauc's relation: $(\alpha h\nu)^{1/n} = A(h\nu - E_g)$ where, $h\nu$ is the incident photon energy, A is a constant and n is the exponent, the value of which is determined by the type of electronic transition causing the absorption and can take the
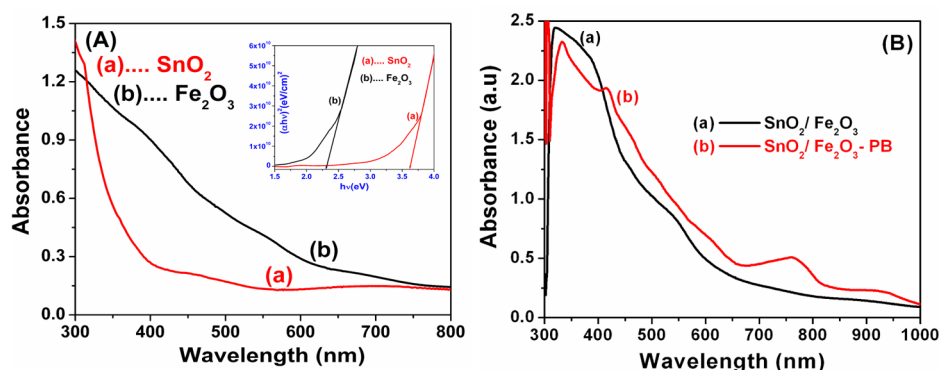
Figure 4. (A) UV−vis absorption spectra of (a) SnO_2 and (b) α-Fe_2O_3 thin films (inset, Tauc plot). (B) UV−vis absorption spectra of (a) SnO_2/α-Fe_2O_3 and (b) SnO_2/α-Fe_2O_3−PB thin films.
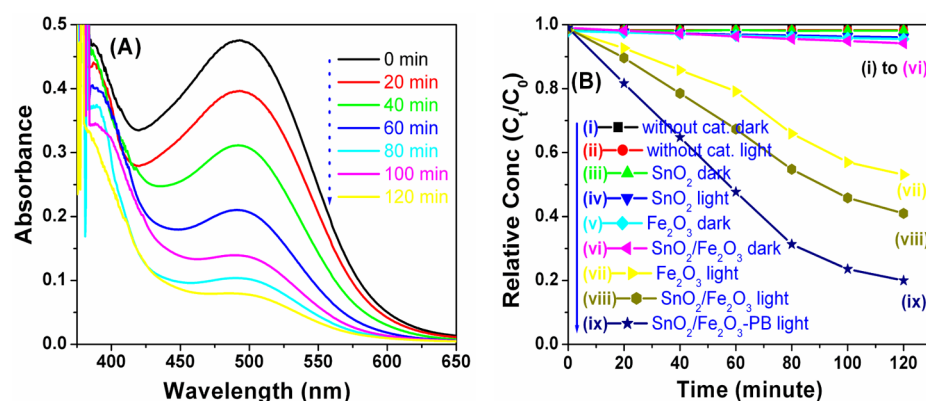

Figure 5. (A) Time-dependent spectral change of Congo red dye solution in the presence of light for SnO_2/α-Fe_2O_3−PB modified thin films. (B) Photodegradation of Congo red in different conditions: (i) without catalyst in dark, (ii) without catalyst in light, (iii) SnO_2 thin films in dark, (iv) SnO_2 thin films in light, (v) α-Fe_2O_3 thin films in dark, (vi) SnO_2/α-Fe_2O_3 thin films in dark, (vii) α-Fe_2O_3 thin films in light, (viiii) SnO_2/α-Fe_2O_3 thin films in light, and (ix) SnO_2/α-Fe_2O_3−PB thin films in light.

values 1/2 or 2 depending upon whether the transition is direct or indirect, respectively. Because SnO_2 is well-established as a direct band gap semiconductor, the E_g value was calculated to 3.6 eV (inset of Figure 4A).

Figure 4A(b) represents the UV−vis spectrum of TCO/α-Fe_2O_3 thin film. A sharp rise in absorbance was appeared from ~550 nm. Optical band gap was calculated from the absorbance data by plotting $(\alpha h\nu)^2$ versus $h\nu$ and extrapolating the linear portion of the curve to the x-axis; α being the absorption coefficient and $h\nu$ the photon energy. The direct band gap (E_g) measured from the absorption value and found to be 2.3 eV, Figure 4B depicts the UV−vis absorption spectra of SnO_2/α-Fe_2O_3 and SnO_2/α-Fe_2O_3−PB modified thin films. In the case of SnO_2/α-Fe_2O_3, a significant absorbance was observed from ~600 nm (Figure 4B(a)) compare to TCO/α-Fe_2O_3, whereas for SnO_2/α-Fe_2O_3−PB (Figure 4B(b)), the mixed-valence charge-transfer band of the polymeric (Fe^{II}−CN−Fe^{III}) sequence at 770 nm was detected along with other two bands at 315 and 430 nm. This is in accordance to the previous report for "PB" by Pyrasch et al.[39] So, the above study revels that in the modified material (SnO_2/α-Fe_2O_3−PB) PB is surely present.

The chemical compositions and the electronic structures of the heterostructures were further analyzed by X-ray photo-emission spectroscopy (XPS). Figure S3 in the Supporting Information shows the XPS spectra of SnO_2/α-Fe_2O_3 and SnO_2/α-Fe_2O_3−PB thin films. Figure S3A in the Supporting Information is the wide range spectra of both films. From this

spectra, it is clear that compare to SnO_2/α-Fe_2O_3 (a), SnO_2/α-Fe_2O_3−PB shows two distinctive peaks of N (N 1s) and C (C 1s) at 396 and 289 eV, respectively. This indicates the presence of −CN groups into SnO_2/α-Fe_2O_3−PB modified hetero-structure, in accordance to similar observation by Zhao et al.[40] The detailed Fe 2p, Sn 3d, O 1s spectra is shown in Figure S3B−D in the Supporting Information. Figure S3B is the XPS spectra of Fe 2p for both films, in which two peaks at 710.7 and 726 eV represents the binding energies of Fe $2p_{3/2}$ and Fe $2p_{1/2}$, respectively.[41] It is interesting to note that after PB incorporation into SnO_2/α-Fe_2O_3 heterostructure (curve b in Figure B), a weak shoulder of the Fe $2p_{3/2}$ peak appears at 707.3 eV. This indicates the existence of Fe^{2+} ions in Prussian blue.[42] So, from the XPS study it can be easily concluded that the ferrous ions certainly comes from PB. Figure S3C in the Supporting Information represents that the binding energies of Sn $3d_{5/2}$ and Sn $3d_{3/2}$ are found at 486 and 496 eV, respectively.[43] The peak centered at 530 eV shows the binding energy of O 1s (Figure S3D in the Supporting Information), which indicates a normal state of O^{2-} in the compounds.[43,44]

To prove again the heterostructure of the prepared thin films, we carried out $I-V$ measurements. The details have been incorporated in the Supporting Information. From the $I-V$ plot (see Figure S4 in the Supporting Information), it is clear that all the composites are n type semiconductor. In addition, the linearity of $I-V$ curves at $V_{ds} = 0$ suggests that ohomic contacts are formed for all the thin films. Now, SnO_2/α-Fe_2O_3−PB and SnO_2/α-Fe_2O_3 shows a distinct change in $I-V$ behavior than
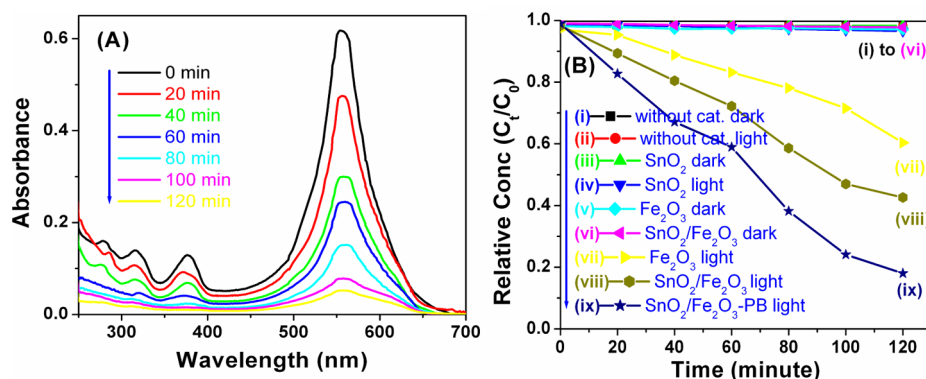
Figure 6. (A) Time-dependent spectral change of rhodamine B dye solution in the presence of light for SnO_2/α-Fe_2O_3−PB modified thin films. (B) Photodegradation of rhodamine B in different conditions: (i) without catalyst in dark, (ii) without catalyst in light, (iii) SnO_2 thin films in dark, (iv) SnO_2 thin films in light, (v) α-Fe_2O_3 thin films in dark, (vi) SnO_2/α-Fe_2O_3 thin films in dark, (vii) α-Fe_2O_3 thin films in light, (viiii) SnO_2/α-Fe_2O_3 thin films in light, (ix) SnO_2/α-Fe_2O_3−PB thin films in light.

other. From the figure, it is clear that SnO_2/α-Fe_2O_3−PB shows the largest photocurrent compared to those of $SnO_2/$ α-Fe_2O_3, α-Fe_2O_3, and SnO_2. This indicates the heterostructure generated due to "PB" incorporation is much effective for the displacement of carriers (electrons). The better electrical conductivity helps in more efficient electron transfer from C_B of Fe_2O_3 to C_B of SnO_2 of SnO_2/α-Fe_2O_3 and "PB"-treated SnO_2/α-Fe_2O_3.

3.1. Photodegradation of Congo Red and Rhodamine B. The photocatalytic degradation of Congo red (CR) dye was investigated with the synthesized materials at ambient temperature. The light irradiation was carried out from a 200 W tungsten lamp (≥410 nm) and a 1 M solution of $NaNO_2$ was used as the UV cutoff filter.[45] The details have been discussed in the Supporting Information. From Figure 5A, it is clear that maximum absorption occurs at ∼495 nm, which is the λ_{max} of CR. The absorption decreases gradually with irradiation time. Figure 5B represents the visible-light dependent photodegradation of Congo red in different conditions. The aqueous solution of CR (3×10^{-4} M) was subjected to a series of experimental conditions: (i) without catalyst in dark, (ii) without catalyst in light, (iii) SnO_2 thin films in dar,k (iv) SnO_2 thin films in light, (v) α-Fe_2O_3 thin films in dark, (vi) SnO_2/α-Fe_2O_3 thin films in dark, (vii) α-Fe_2O_3 thin films in light, (viiii) SnO_2/α-Fe_2O_3 thin films in light, (ix) SnO_2/α-Fe_2O_3−PB thin films in light. There was no degradation in dark for SnO_2, α-Fe_2O_3 and SnO_2/α-Fe_2O_3 thin films and also by using SnO_2 thin films in light no degradation was detected because of its wide band gap. In the presence of light, only 44% degradation was observed for Fe_2O_3 thin films. On the contrary, for the coupled system, i.e., SnO_2/α-Fe_2O_3 in the presence of light, a recognizable degradation was found and the efficiency was increased to 59%. This percentage of degradation increased enormously when it was again modified with prussian blue (PB). For SnO_2/α-Fe_2O_3−PB modified thin films, an efficiency of ∼80% was achieved.

Photocatalytic activity of the synthesized thin films was again investigated for rhodamin-B (RhB) dye degradation. Similarly, four thin films of active surface area 2 × 1 cm^2 were vertically placed into 50 mL (3×10^{-4} M) RhB solution. Figure 6A shows the absorption spectra of RhB in the presence of $SnO_2/$ α-Fe_2O_3−PB modified thin films. It is clear that maximum absorption occurs at ∼556 nm which is the λ_{max} of RhB and the intensity decreases gradually with irradiation time. Figure 6B

represents photodegradation of RhB in different conditions. The visible-light induced photocatalytic activity of (i) without catalyst in dark, (ii) without catalyst in light, (iii) SnO_2 thin films in dark, (iv) SnO_2 thin films in light, (v) α-Fe_2O_3 thin films in dark, (vi) SnO_2/α-Fe_2O_3 thin films in dark, (vii) α-Fe_2O_3 thin films in light, (viiii) SnO_2/α-Fe_2O_3 thin films in light, (ix) SnO_2/α-Fe_2O_3−PB thin films in light was investigated. Here also, no such photodegradation of RhB was detected for SnO_2, α-Fe_2O_3, and SnO_2/α-Fe_2O_3 thin films in dark and SnO_2 in light. From Figure 6B, it is clear that in the presence of light about 40% degradation was observed for α-Fe_2O_3 thin films and the coupled form, i.e., SnO_2/α-Fe_2O_3 thin films showed about 58% of degradation in the presence of light. This efficiency was increased to ∼82% for the modified system (SnO_2/α-Fe_2O_3−PB) in the presence of light.

The enhanced reactivity of the coupled semiconductor could be explained by its band diagram.[46,47] Under light irradiation, the photogenerated electrons on the conduction band (CB) of Fe_2O_3 transfer to the CB of SnO_2 to decrease the potential energy[48] and the holes on valence band (VB) of SnO_2 transfer to the VB of Fe_2O_3 simultaneously. This unique behavior of the heterostructures enables the separation of the photogenerated electrons and holes and reduces recombination probability and increases their mobilities. The photogenerated hole on the VB of Fe_2O_3 is less anodic than SnO_2 and the CB electron in photo excited SnO_2 is less cathodic than that of Fe_2O_3. This difference in edge potentials between SnO_2 and Fe_2O_3 leads to separation of photogenerated charge carriers across the heterojunction, which enhances the photocatalytic activity. Schematic representation of the band diagram for photocatalytic degradation under visible light irradiation is illustrated in Figure S5 in the Supporting Information.

The essential requirement is separation of electrons (e^-) and holes (h^+) by absorbing light. The photo generated electrons and holes react with adsorbed surface substances, like O_2, OH^- and form reactive species O_2^-, OH^* (hydroxyl radicals). These oxidative species degrade the organic substance into small molecules like CO_2, H_2O, NO_3^-, NH_4^+ etc.[49] In the absence of electron acceptors (O_2), there is a great chance of electron hole recombination.

Again higher photocatalytic activity of PB-modified system, i.e., SnO_2/α-Fe_2O_3−PB (for both cases) might be due to rapid electron transfer due to addition of necessary ferrous ions into Fe_2O_3 which accelerate catalytic reaction to a large extent.[13]

The largest photocurrent generated by SnO_2/α-Fe_2O_3–PB (from I–V measurement) also confirms that the heterostructure generated due to "PB" incorporation is much effective for the displacement of carriers (electrons). In addition, "PB" exhibits excellent electrochemical behavior that can accelerate the electron transfer and results high catalytic activity.[13,48]

3.2. Hydroxyl Radical Formation.
From the photocatalytic study, it can be concluded that the activity (to degrade/decompose organic dyes) of a particular material will be higher if it generates reactive species (O_2^-, OH^*) at higher rate.[50] The hydroxyl radical performs the key role for the decomposition of the organic pollutants. So it is necessary to investigate the amount of hydroxyl radicals produced by each photocatalyst during the reaction. The general technique has been used here to establish the hydroxyl radical formation by different thin films where terephthalic acid (TPA) was taken as a probe molecule. In this method, TPA was directly attacked by a OH radical and forms 2-hydroxyterephthalic acid, which gives a fluorescence signal at 426 nm.[51,52] Figure S6 in the Supporting Information depicts the fluorescent signal of the photocatalysts (SnO_2, α-Fe_2O_3, SnO_2/α-Fe_2O_3, SnO_2/α-Fe_2O_3–PB thin films) after reacting with TPA solution. The fluorescent intensity is directly related to the number of hydroxyl radicals formed by each photocatalysts. It means the higher the rate of hydroxyl radicals, the greater the yield of TPAOH and the more intense the fluorescence peak. Here, SnO_2/Fe_2O_3–PB with the highest fluorescence intensity confirms the generation of a greater number of hydroxyl radicals than other. The fluorescence intensity follows the trend $SnO_2 < \alpha$-$Fe_2O_3 < SnO_2/\alpha$-$Fe_2O_3 < SnO_2/\alpha$-Fe_2O_3–PB.

To prove the stability of Prussian blue "PB" after photodegradation (in CR and RhB) XRD spectra was investigated. Figure S7 (see the Supporting Information) represents the XRD pattern of SnO_2/α-Fe_2O_3–PB thin film after photodegradation in (A) Congo red (CR) (B) Rhodamine B (RhB). From the XRD spectra, it can be concluded that existence of "PB" is sound enough in the modified heterostructure, even after photodegradation experiment.

3.3. Evaluation of Electrocatalytic Activities.
The electrocatalytic activities of the thin films (modified on TCO) were monitored by cyclic voltammetric (CV) technique. H_2O_2 was taken as a model compound because identification of H_2O_2, a product of enzymatic reactions is important in the development of biosensor.[53]

Electrocatalytic measurements were carried out in 0.05 M phosphate buffer solution (PBS) at pH 7.0. SnO_2/α-Fe_2O_3–PB thin film was taken as an working electrode and a platinum wire, an Ag/AgCl were used as auxiliary and reference electrodes, respectively. The amperometric response of SnO_2/α-Fe_2O_3–PB was carried out at different conditions (varying pH and temperature) and compared with that of bare SnO_2 and SnO_2/α-Fe_2O_3 thin films. The current response due to the addition of H_2O_2 was monitored. The apparent Michaelis–Menten constant, K_M^{app} and the maximum current of SnO_2/α-Fe_2O_3 and SnO_2/α-Fe_2O_3–PB electrodes can be determined from the Michaelis–Menten equation.[54]

$$I = (I_{max}[S])/(K_M^{app} + [S]) \quad (8)$$

Where I represent the steady-state current, I_{max}, the maximum current measured under conditions of enzyme saturation, and [S] the concentration of substrate. Rearrangement of the Michaelis–Menten equation as follows

$$1/I = 1/I_{max} + K_M^{app}/(I_{max}[S]) \quad (9)$$

yields the electrochemical version of the Lineweaver–Burk equation, which also enables the analysis of the enzyme kinetics.

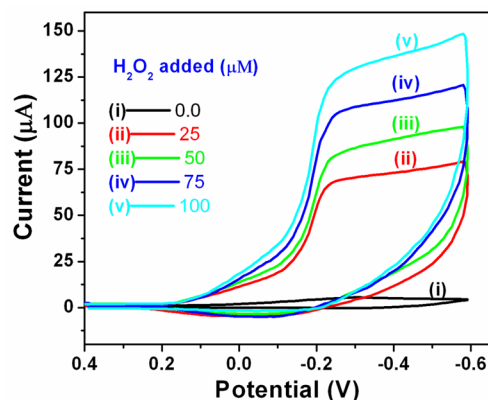### 3.4. Performance of SnO_2/α-Fe_2O_3–PB Thin Films toward Reduction of H_2O_2.
Figure 7 shows the cyclic

Figure 7. Cyclic voltamogram of SnO_2/α-Fe_2O_3–PB electrode in 0.05 M PBS (pH 7.0) containing (i) 0, (ii) 25, (iii) 50, (iv) 75, and (v) 100 μM H_2O_2 at 0.1 V s-1 (vs Ag/AgCl).

voltamograms of SnO_2/α-Fe_2O_3–PB at pH 7.0 with varying H_2O_2 concentrations. The first CV scan was taken without adding H_2O_2 into the buffer solution. With increasing concentration of H_2O_2, a steady increase of current height in the cathodic sweep indicates that the modified electrode has electrocatalytic property to the reduction of H_2O_2. At -0.23 V, a cathodic peak was detected.

3.5. Amperometric Responses of H_2O_2 Sensor.
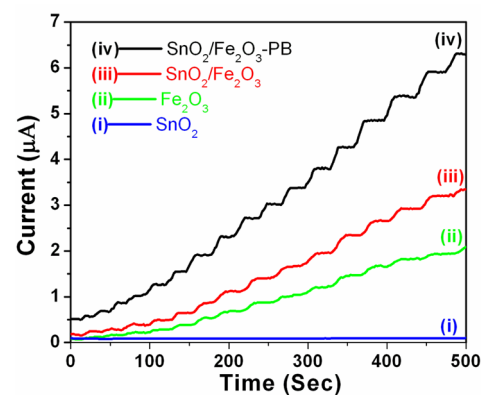Figure 8 depicts the typical steady-state amperometric responses of

Figure 8. Amperometric responses of (i) SnO_2, (ii) α-Fe_2O_3, (iii) SnO_2/α-Fe_2O_3, (iv) SnO_2/α-Fe_2O_3–PB upon successive addition of different amounts of H_2O_2 to PBS.

SnO_2, α-Fe_2O_3, SnO_2/α-Fe_2O_3, and SnO_2/α-Fe_2O_3–PB at constant potential (-0.23 V) with the gradual addition of H_2O_2. When an aliquot of H_2O_2 was added to the PBS (pH 7.0), the reduction current increases sharply to reach a steady-state value (ca. 95%) in less than 8 s. However, in case of SnO_2 electrode, no significant current response was detected. To obtain the calibration curves for α-Fe_2O_3, SnO_2/α-Fe_2O_3, and SnO_2/α-Fe_2O_3–PB electrodes (Figure 9A), we plotted the steady-state current values against concentration of H_2O_2. A

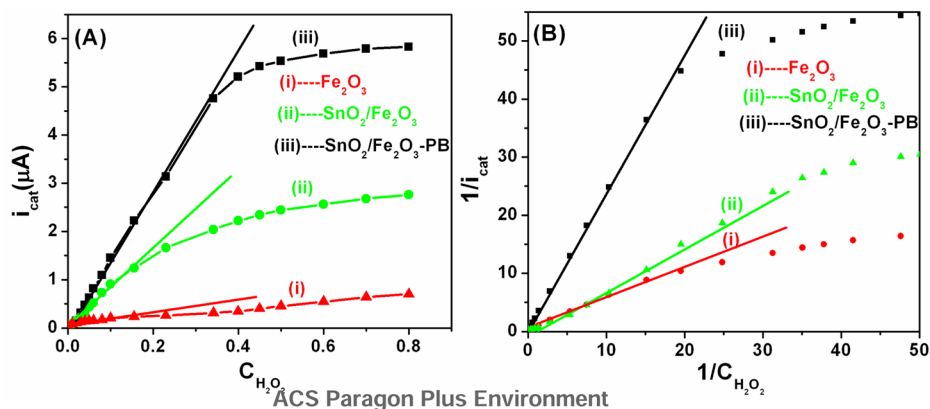**Figure 9.** (A) Calibration curves for (i) α-Fe$_2$O$_3$, (ii) SnO$_2$/α-Fe$_2$O$_3$, and (iii) SnO$_2$/α-Fe$_2$O$_3$−PB thin films showing Michaelis−Menten type behavior. (B) Lineweaver−Burk plot of these elesctrodes.

linear relationship was observed in the concentration range of 20−332 μM (correlation coefficient 0.9864) with a sensitivity of 8.70 μAm M^{-1} for SnO$_2$/α-Fe$_2$O$_3$−PB electrode, whereas for SnO$_2$/α-Fe$_2$O$_3$, the linear range was found to 20−165 μM (correlation coefficient 0.97419) and sensitivity was calculated to 3.86 μA mM^{-1}. A comparatively lower linear range of 20−150 μM and poor sensitivity (1.04 μA mM^{-1}) was calculated for α-Fe$_2$O$_3$ electrode. The detection limits were also estimated for the above-mentioned electrodes and were found to be 0.27, 0.28, and 0.24 μM for SnO$_2$/α-Fe$_2$O$_3$−PB, SnO$_2$/α-Fe$_2$O$_3$, and α-Fe$_2$O$_3$ electrodes, respectively (signal-to-noise ratio = 3).

As shown in Figure 9A, the calibration curves also illustrate Michaelis−Menten type behavior. According to the electrochemical version of Lineweaver−Burk model, the apparent Michaelis−Menten constants (K_M^{app}) were calculated (Figure 9B) and found 0.367, 0.675, and 1.187 mM for SnO$_2$/α-Fe$_2$O$_3$−PB, SnO$_2$/α-Fe$_2$O$_3$, and α-Fe$_2$O$_3$ electrodes, respectively. The smaller K_M^{app} value of SnO$_2$/α-Fe$_2$O$_3$−PB indicates that it has higher affinity toward sensing of H$_2$O$_2$ than that of SnO$_2$/α-Fe$_2$O$_3$.

To use SnO$_2$, α-Fe$_2$O$_3$, SnO$_2$/α-Fe$_2$O$_3$, and SnO$_2$/α-Fe$_2$O$_3$−PB thin films as electrochemical sensors for H$_2$O$_2$ detection, they were used separately as the working electrode in the experiment. Preliminary studies have revealed that over the pH range 2.0−10.0 and the temperature from 20 to 80 °C, maximum electrocatalytic decomposition of H$_2$O$_2$ occurs at pH 7.0 and 40 °C (see Figure S8 in the Supporting Information).

4. CONCLUSIONS

SnO$_2$/α-Fe$_2$O$_3$ heterostructure thin films were successfully synthesized by galvanic and chemical deposition techniques. Fe$_2$O$_3$ is a narrow band gap semiconductor and it has short hole diffusion length. Combining Fe$_2$O$_3$ to SnO$_2$ results an effective photocatalyst to degrade Congo red and Rhodamine B dye. Again, chemical modification of coupled system (extra ferrous ion incorporation into SnO$_2$/α-Fe$_2$O$_3$) results in higher photocatalytic activity than SnO$_2$/α-Fe$_2$O$_3$, because of better electron transfer that accelerates the easy separation of electrons and holes. The fast production of OH radical (by PL measurement) reveals the greater ability of the modified heterostructures (SnO$_2$/α-Fe$_2$O$_3$−PB) to degrade organic dyes. Electrocatalytic study also confirms that the modified heterostructures have higher affinity toward the sensing of H$_2$O$_2$. High sensitivity, long linear range, etc., are the pronounced features of this modified sensor. So, our

synthesized SnO$_2$/Fe$_2$O$_3$−PB thin films could not only be used as an effective photocatalyst to degrade organic dyes but can also be used as an effective peroxide sensor.

■ ASSOCIATED CONTENT

Ⓢ Supporting Information

Materials and instruments, phocatalytic activities, photographs of thin films (Figure S1), EDX (Figure S2), XPS (Figure S3), I−V (Figure S4), band diagram (Figure S5), PL (Figure S6), XRD after photodegradation (Figure S7), and catalytic response of SnO$_2$/α-Fe$_2$O$_3$−PB electrode with pH and temperature (Figure S8). This material is available free of charge via the Internet at http://pubs.acs.org.

■ AUTHOR INFORMATION

Corresponding Author

*E-mail: anupmondal2000@yahoo.co.in. Fax: 91-33-2668-2916.

Notes

The authors declare no competing financial interest.

■ ACKNOWLEDGMENTS

■ REFERENCES

(1) Abe, R.; Takami, H.; Murakami, N.; Ohtani, B. Pristine Simple Oxides as Visible Light Driven Photocatalysts: Highly Efficient Decomposition of Organic Compounds over Platinum-Loaded Tungsten Oxide. *J. Am. Chem. Soc.* **2008**, *130*, 7780−7781.

(2) Qin, H.; Li, W.; Xia, Y.; He, T. Photocatalytic Activity of Heterostructures Based on ZnO and N-Doped ZnO. *ACS Appl. Mater. Interfaces* **2011**, *3*, 3152−3156.

(3) (a) Liu, L.; Li, Y.; Yuan, S. M.; Ge, M.; Ren, M. M.; Sun, C. S.; Zhou, Z. Nanosheet-Based NiO Microspheres: Controlled Solvothermal Synthesis and Lithium Storage Performances. *J. Phys. Chem. C* **2010**, *114*, 251−255. (b) Jana, S.; Samai, S.; Mitra, B. C.; Bera, P.; Mondal, A. Nickel Oxide Thin Film from Electrodeposited Nickel Sulfide Thin Film: Peroxide Sensing and Photo-Decomposition of Phenol. *Dalton Trans.* **2014**, *43*, 13096−13104.

15838

dx.doi.org/10.1021/am5030879 | *ACS Appl. Mater. Interfaces* 2014, 6, 15832−15840

(4) Linsebigler, A. L.; Lu, G.; Yates, J. T. Photocatalysis on TiO₂ Surfaces: Principles, Mechanisms, and Selected Results. *Chem. Rev.* **1995**, *95*, 735–758.

(5) Alam, M.; Cameron, D. C. Optical and Electrical Properties of Transparent Conductive ITO Thin Films Deposited by Sol Gel Process. *Thin Solid Films* **2000**, *377*, 455–459.

(6) Sinha, A. K.; Pradhan, M.; Sarkar, S.; Pal, T. Large-Scale Solid-State Synthesis of Sn−SnO₂ Nanoparticles from Layered SnO by Sunlight: A Material for Dye Degradation in Water by Photocatalytic Reaction. *Environ. Sci. Technol.* **2013**, *47*, 2339–2345.

(7) Long, Y. Z.; Lu, Y.; Huang, Y.; Peng, Y. C.; Lu, Y.; Kang, S. Z.; Mu, J. Effect of C60 on the Photocatalytic Activity of TiO₂ Nanorods. *J. Phys. Chem. C* **2009**, *113*, 13899–13905.

(8) Han, Y. T.; Wu, X.; Shen, G. Z.; Dierre, B.; Gong, L. H.; Qu, F. Y.; Bando, Y.; Sekiguchi, T.; Fabbri, F.; Golberg, D. Solution Growth and Cathodoluminescence of Novel SnO₂ Core−Shell Homogeneous Microspheres. *J. Phys. Chem. C* **2010**, *114*, 8235–8240.

(9) Lee, W. J.; Park, M. H.; Wang, Y.; Lee, J. Y.; Cho, J. Nanoscale Si Coating on the Pore Walls of SnO₂ Nanotube Anode for Li Rechargeable Batteries. *Chem. Commun.* **2010**, *46*, 622–624.

(10) Duong, T. T.; Choi, H. J.; He, Q. J.; Le, A. T.; Yoon, S. G. Enhancing the Efficiency of Dye Sensitized Solar Cells with an SnO₂ Blocking Layer Grown by Nanocluster Deposition. *J. Alloys Compd.* **2013**, *561*, 206–210.

(11) Mohamed, S. H. SnO₂ Dendrites−Nanowires for Optoelectronic and Gas Sensing Applications. *J. Alloys Compd.* **2012**, *510*, 119–124.

(12) Uchiyama, H.; Nagao, R.; Kozuka, H. Photoelectrochemical Properties of ZnO−SnO₂ Films Prepared by Sol−Gel Method. *J. Alloys Compd.* **2013**, *554*, 122–126.

(13) Zhang, L. Z.; Yu, J. C. A Sonochemical Approach to Hierarchical Porous Titania Spheres with Enhanced Photocatalytic Activity. *Chem. Commun.* **2003**, 2078–2079.

(14) Han, Y.; Wu, X.; Ma, Y.; Gong, L.; Qu, F.; Fan, H. Porous SnO₂ Nanowire Bundles for Photocatalyst and Li Ion Battery Applications. *CrystEngComm* **2011**, *13*, 3506–3510.

(15) Wu, S.; Cao, H.; Yin, S.; Liu, X.; Zhang, X. Amino Acid-Assisted Hydrothermal Synthesis and Photocatalysis of SnO₂ Nanocrystals. *J. Phys. Chem. C* **2009**, *113*, 17893–17898.

(16) Le Formal, F.; Gratzel, M.; Sivula, K. Controlling Photoactivity in Ultrathin Hematite Films for Solar Water-Splitting. *Adv. Funct. Mater.* **2010**, *20*, 1099–1107.

(17) Kay, A.; Cesar, I.; Gratzel, M. New Benchmark for Water Photooxidation by Nanostructured α-Fe₂O₃ Films. *J. Am. Chem. Soc.* **2006**, *128*, 15714–15721.

(18) Zhong, D. K.; Sun, J.; Inumaru, H.; Gamelin, D. R. Solar Water Oxidation by Composite Catalyst/α-Fe₂O₃ Photoanodes. *J. Am. Chem. Soc.* **2009**, *131*, 6086–6087.

(19) Batzill, M.; Diebold, U. The Surface and Materials Science of Tin Oxide. *Prog. Surf. Sci.* **2005**, *79*, 47–154.

(20) Law, M.; Kind, H.; Messer, B.; Kim, F.; Yang, P. D. Photochemical Sensing of NO₂ with SnO₂ Nanoribbon Nanosensors at Room Temperature. *Angew. Chem.* **2002**, *41*, 2405–2408.

(21) Kuang, Q.; Lao, C. S.; Wang, Z. L.; Xie, Z. X.; Zheng, L. S. High-Sensitivity Humidity Sensor Based on a Single SnO₂ Nanowire. *J. Am. Chem. Soc.* **2007**, *129*, 6070–6071.

(22) Zhang, D. F.; Sun, L. D.; Jia, C. J.; Yan, Z. G.; You, L. P.; Yan, C. H. Hierarchical Assembly of SnO₂ Nanorod Arrays on α-Fe₂O₃ Nanotubes: A Case of Interfacial Lattice Compatibility. *J. Am. Chem. Soc.* **2005**, *127*, 13492–13493.

(23) Tan, O. K.; Zhu, W.; Yan, Q.; Kong, L. B. Size Effect and Gas Sensing Characteristics of Nanocrystalline xSnO₂−(1-x)α-Fe₂O₃ Ethanol Sensors. *Sens. Actuators, B* **2000**, *65*, 361–365.

(24) Rumyantseva, M. N.; Kovalenko, V. V.; Gaskov, A. M.; Pagnier, T.; Machon, D.; Arbiol, J.; Morante, J. R. Nanocomposites SnO₂/Fe₂O₃:Wet Chemical Synthesis and Nanostructure Characterization. *Sens. Actuators, B* **2005**, *109*, 64–74.

(25) Patil, L. A.; Shinde, M. D.; Bari, A. R.; Deo, V. V.; Patil, D. M.; Kaushik, M. P. Fe₂O₃ Modified Thick Films of Nanostructured SnO₂ Powder Consisting of Hollow Microspheres Synthesized from Pyrolysis of Ultrasonically Atomized Aerosol for LPG Sensing. *Sens. Actuators, B* **2011**, *155*, 174–182.

(26) Chen, Y. J.; Zhu, C. L.; Wang, L. J.; Gao, P.; Cao, M. S.; Shi, X. L. Synthesis and Enhanced Ethanol Sensing Characteristics of α-Fe₂O₃/SnO₂ Core−Shell Nanorods. *Nanotechnology* **2009**, *20*, 045502–045508.

(27) Niu, M.; Huang, F.; Cui, L.; Huang, P.; Yu, Y.; Wang, Y. Hydrothermal Synthesis, Structural Characteristics, and Enhanced Photocatalysis of SnO₂/α-Fe₂O₃ Semiconductor Nanoheterostructures. *ACS Nano* **2010**, *4*, 681–688.

(28) Sorescu, M.; Diamandescu, L.; Tomescu, A.; Tarabasanu-Mihaila, D.; Teodorescu, V. Structure and Sensing Properties of 0.1 SnO₂−0.9 α-Fe₂O₃ System. *Mater. Chem. Phys.* **2008**, *107*, 127–131.

(29) Kang, J.; Kuang, Q.; Xie, Z. X.; Zheng, L. S. Fabrication of the SnO₂/α-Fe₂O₃ Hierarchical Heterostructure and Its Enhanced Photocatalytic Property. *J. Phys. Chem. C* **2011**, *115*, 7874–7879.

(30) Burda, C.; Chen, X. B.; Narayanan, R.; El-Sayed, M. A. Chemistry and Properties of Nanocrystals of Different Shapes. *Chem. Rev.* **2005**, *105*, 1025–1102.

(31) Astruc, D.; Lu, F.; Aranzaes, J. R. Nanopartikel als Regenerierbare Katalysatoren: an der Nahtstelle Zwischen Homogener und Heterogener Katalyse. *Angew. Chem.* **2005**, *117*, 8062–8083.

(32) Fiorito, P. A.; Goncales, V. R.; Ponzio, E. A.; Torresi, S. I. C. D. Synthesis, Characterization and Immobilization of Prussian Blue Nanoparticles. A Potential Tool for Biosensing Devices. *Chem. Commun.* **2005**, 366–368.

(33) Zhuo, Y.; Yuan, P. X.; Yuan, R.; Chai, Y. Q.; Hong, C. L. Bienzyme Functionalized Three-Layer Composite Magnetic Nanoparticles for Electrochemical Immunosensors. *Biomaterials* **2009**, *30*, 2284–2290.

(34) Sun, E. Y.; Josephson, L.; Kelly, K. A.; Weissleder, R. Development of Nanoparticle Libraries for Biosensing. *Bioconjugate Chem.* **2006**, *17*, 109–113.

(35) Jana, S.; Mitra, B. C.; Bera, P.; Sikdar, M.; Mondal, A. Photocatalytic Activity of Galvanically Synthesized Nanostructure SnO₂ Thin Films. *J. Alloys Compd.* **2014**, *602*, 42–48.

(36) Bhar, S. K.; Mukherjee, N.; Maji, S. K.; Adhikary, B.; Mondal, A. Synthesis of Nanocrystalline Iron Oxide Ultrathin Films by Thermal Decomposition of Iron Nitropruside: Structural and Optical Properties. *Mater. Res. Bull.* **2010**, *45*, 1948–1953.

(37) Kumar, A. V. N.; Joseph, J. Selective Patterning of Prussian Blue on N-[3-(trimethoxysilyl)propyl]ehylenediamine Capped Gold Nanoparticle Film for Electrocatalysis of Hydrogen Peroxide Reduction. *RSC Adv.* **2014**, *4*, 10975–10981.

(38) Zhang, X. Q.; Gong, S. W.; Zhang, Y.; Yang, T.; Wang, C. Y.; Gu, N. Prussian Blue Modified Iron Oxide Magnetic Nanoparticles and Their High Peroxidase-like Activity. *J. Mater. Chem.* **2010**, *20*, 5110–5116.

(39) Pyrasch, M.; Tieke, B. Electro-and Photoresponsive Films of Prussian Blue Prepared upon Multiple Sequential Adsorption. *Langmuir* **2001**, *17*, 7706–7709.

(40) Zhao, G.; Feng, J. J.; Zhang, Q. L.; Li, S. P.; Chen, H. Y. Synthesis and Characterization of Prussian Blue Modified Magnetite Nanoparticles and Its Application to the Electrocatalytic Reduction of H₂O₂. *Chem. Mater.* **2005**, *17*, 3154–3159.

(41) Chen, Y. J.; Gao, X. M.; Di, X. P.; Ouyang, Q. Y.; Gao, P.; Qi, L. H.; Li, C. Y.; Zhu, C. L. Porous Iron Molybdate Nanorods: In situ Diffusion Synthesis and Low-Temperature H₂S Gas Sensing. *ACS Appl. Mater. Interfaces* **2013**, *5*, 3267–3274.

(42) Yatsimirskii, K. B.; Nemoshalenko, V. V.; Nazarenko, Y. P.; Aleshin, V. G.; Zhilinskaya, V. V.; Tomashevsky, N. A. Use of X-ray Photoelectron and Mössbauer Spectroscopies in the Study of Iron Pentacyanide Complexes. *J. Electron Spectrosc. Relat. Phenom.* **1977**, *10*, 239–245.

(43) Liu, L.; Li, S.; Wang, L.; Guo, C.; Dong, Q.; Li, W. Enhancement Ethanol Sensing Properties of NiO−SnO₂ Nanofibers. *J. Am. Ceram. Soc.* **2011**, *94*, 771–775.

(44) Ahn, H. J.; Choi, H. C.; Park, K. W.; Kim, S. B.; Sung, Y. E. Investigation of the Structural and Electrochemical Properties of Size-Controlled SnO_2 Nanoparticles. *J. Phys. Chem. B* **2004**, *108*, 9815−9820.

(45) Ikbal, M.; Banerjee, R.; Atta, S.; Dhara, D.; Anoop, A.; Singh, N. D. P. Synthesis, Photophysical and Photochemical Properties of Photoacid Generators Based on N-Hydroxyanthracene-1,9-dicarboxyimide and Their Application toward Modification of Silicon Surfaces. *J. Org. Chem.* **2012**, *77*, 10557−10567.

(46) Xu, Y.; Schoonen, M. A. A. The Absolute Energy Positions of Conduction and Valence Bands of Selected Semiconducting Minerals. *Am. Mineral.* **2000**, *85*, 543−556.

(47) Trani, F.; Causà, M.; Ninno, D.; Cantele, G.; Barone, V. Density Functional Study of Oxygen Vacancies at the SnO_2 Surface and Subsurface Sites. *Phys. Rev. B* **2008**, *77*, 245410−245418.

(48) Wu, W.; Zhang, S. F.; Xiao, X. H.; Zhou, J.; Ren, F.; Sun, L. L.; Jiang, C. Z. Controllable Synthesis, Magnetic Properties, and Enhanced Photocatalytic Activity of Spindle like Mesoporous α-Fe_2O_3/ZnO Core−Shell Heterostructures. *ACS Appl. Mater. Interfaces* **2012**, *4*, 3602−3609.

(49) Lachheb, H.; Puzenat, E.; Houas, A.; Ksibi, M.; Elaloui, E.; Guillard, C.; Herrmann, J. M. Photocatalytic Degradation of Various Types of Dyes (Alizarin S, Crocein Orange G, Methyl Red, Congo Red, Methylene Blue) in Water by UV-Irradiated Titania. *Appl. Catal., B* **2002**, *39*, 75−90.

(50) Sun, E. Y.; Josephson, L.; Kelly, K. A.; Weissleder, R. Development of Nanoparticle Libraries for Biosensing. *Bioconjugate Chem.* **2006**, *17*, 109−113.

(51) Liu, G.; Niu, P.; Yin, L.; Cheng, H. M. α-Sulfur Crystals as a Visible-Light-Active Photocatalyst. *J. Am. Chem. Soc.* **2012**, *134*, 9070−9073.

(52) Hirakawa, T.; Nosaka, Y. Properties of $O_2^{\cdot-}$ and OH· Formed in TiO_2 Aqueous Suspensions by Photocatalytic Reaction and the Influence of H_2O_2 and Some Ions. *Langmuir* **2002**, *18*, 3247−3254.

(53) Salimi, A.; Hallaj, R.; Soltanian, S.; Mamkhezri, H. Nanomolar Detection of Hydrogen Peroxide on Glassy Carbon Electrode Modified with Electrodeposited Cobalt Oxide Nanoparticles. *Anal. Chim. Acta* **2007**, *594*, 24−31.

(54) Kamin, R. A.; Willson, G. S. Rotating Ring-Disk Enzyme Electrode for Biocatalysis Kinetic Studies and Characterization of the Immobilized Enzyme Layer. *Anal. Chem.* **1980**, *52*, 1198−1205.

15840

dx.doi.org/10.1021/am5030879 | *ACS Appl. Mater. Interfaces* 2014, 6, 15832−15840